PAPER

Check for updates

Red-emissive carbon quantum dots enable high efficiency luminescent solar concentrators†

Guiju Liu, [ID] *[abc] Margherita Zavelani-Rossi, [ID] [d] Guangting Han,[a] Haiguang Zhao [ID] *[a] and Alberto Vomiero*[ce]

Luminescent solar concentrators (LSCs) are large-area sunlight collectors for efficient solar-to-electricity conversion. The key point for highly efficient LSCs is the choice of fluorophores, which need to have broad absorption, high quantum yield and large Stokes shift. Among various fluorophores, carbon quantum dots (C-dots) hold great promise as eco-friendly alternatives to heavy-metal-containing quantum dots (QDs) due to their adjustable absorption and emission spectra, non-toxicity, low cost and eco-friendly synthetic methods. However, due to the limited absorption band and relatively low quantum yield in the red region, it is a challenge to obtain efficient LSCs based on C-dots. Here, we demonstrated highly efficient LSCs based on red-emissive C-dots. The as-synthesized C-dots have a cubic structure, broad absorption covering 300−600 nm, and red emission (peak located at 595 nm), with a high quantum yield of ∼65% and a large Stokes shift of 0.45 eV. Transient absorption experiments of the C-dots revealed the ultrafast formation of the broad emissive state (1 ps). Based on the excellent optical properties of the C-dots, the as-prepared large-area LSC (10 × 10 × 0.52 cm³) exhibited an optimized external optical efficiency of 4.81% and a power conversion efficiency of 2.41% under natural sun irradiation (70 mW cm⁻²). Furthermore, a tandem LSC using green-emissive C-dots (top layer) and red-emissive C-dots (bottom layer) as fluorophores exhibited an external optical efficiency as high as 6.78%. These findings demonstrate the possibility of using eco-friendly carbon-based nanomaterials for highly efficient large-area LSCs.

Introduction

Due to the world's energy shortage and air pollution, solar technologies have attracted much attention and spurred a rapid development. Among various types of solar technologies, solar electricity is the most common means of using solar energy to address the current energy crisis and climate change.[1–3] However, obtaining high solar-to-electrical power conversion efficiency (PCE) and cost-effective solar cells is still a major challenge in photovoltaic (PV) power generation. Luminescent solar concentrator (LSC) coupling to solar cells is a simple yet efficient technology to collect sunlight and to reduce the cost of electricity.[4,5] A typical LSC consists of an optical waveguide in which suitable fluorophores are homogeneously dispersed. Upon illumination, the fluorophores absorb sunlight from different incident directions and re-emit light at shorter or longer wavelengths through fluorescence. The majority of the emitted light is propagated along the waveguide by total internal reflection and collected into the solar cells attached at the edges of the LSC.[6–8] The LSCs could largely decrease the use of expensive photovoltaic materials due to the small edges compared to the large surface of the LSC. If the overall PCE of the LSC-PV is over 6%, the LSCs could reduce the cost of photovoltaic power generation.[9] The LSC-PV system could be widely used in building-integrated photovoltaics (BIPVs) due to its light weight, high transparency and tunable colors.[10,11] In addition, LSCs are also widely used in dark-field imaging,[12] microreactors,[13] greenhouse coatings[14] and free-space optical communications.[15]

The external optical efficiency of LSCs is defined as the total number of photons emitted from the edges over the total number of photons radiated from the top of the LSCs.[9,16] To obtain high-efficiency LSCs, the key factor is to select high quality fluorophores, which need to have broad absorption well matched with Sun's spectrum, high quantum yield (QY), large Stokes shift with a small overlap between the absorption and emission spectra, and long-term stability.[16] The broad absorption means the fluorophores can absorb more solar energy, the

aCollege of Textiles & Clothing, State Key Laboratory of Bio-Fibers and Eco-Textiles, Qingdao University, No. 308 Ningxia Road, Qingdao 266071, P. R. China. E-mail: hgzhao@qdu.edu.cn

bDepartment of Physics, Yantai University, Yantai 264005, P. R. China. E-mail: gjliu@ytu.edu.cn

cDepartment of Engineering Sciences and Mathematics, Division of Materials Science, Luleå University of Technology, 971 87 Luleå, Sweden. E-mail: alberto.vomiero@ltu.se

dDipartimento di Energia, Politecnico di Milano, via G. Ponzio 34/3 and IFN-CNR, piazza L. da Vinci 32, 20133 Milano, Italy

eDepartment of Molecular Sciences and Nano Systems, Ca' Foscari University of Venice, Via Torino 155, 30172 Venezia Mestre, Italy

† Electronic supplementary information (ESI) available. See DOI: https://doi.org/10.1039/d2ta09972a

8950 | *J. Mater. Chem. A*, 2023, 11, 8950–8960

This journal is © The Royal Society of Chemistry 2023

high QY means the fluorophores can re-emit more photons to transmit to the edges for solar cell absorption, and the large Stokes shift can decrease the reabsorption probability of the re-emitted photons and reduce the energy loss during photon transmission. In recent years, various types of fluorophores have been used for fabricating high performance LSCs.[17–21] Among these fluorophores, colloidal quantum dots (QDs) have attracted a lot of attention due to their size and composition tunable absorption/emission spectra, high QY and excellent stability.[20–23] However, the most efficient QD based LSCs contain toxic elements (Pb or Cd), such as in CdSe/CdS, PbS/CdS or $CsPbCl_xBr_{3-x}$ QDs.[9,17,24,25] Considering the large-scale preparation and practical application, environmental pollution may be a major issue for these heavy-metal-containing QD based LSCs. Recently, a series of eco-friendly heavy-metal-free QDs were synthesized and employed as fluorophores in LSCs, for example $AgInS_2$/ZnS, $CuInS_2$/ZnS, Si QDs and carbon QDs (C-dots).[4,20,26–30] Among them, C-dots have a wide absorption band and tunable emission spectra, an absorption coefficient comparable to inorganic QDs, low cost and good stability, which make them promising candidate fluorophores for LSCs.[30–33] For example, Zhao et al.[30] used C-dots with a high QY and large Stokes shift to prepare LSCs and obtained an external optical efficiency of 2.2% (15×15 cm^2). Zhou et al.[34] reported a laminated LSC based on C-dots with an external optical efficiency of 1.1% (10×10 cm^2). However, these C-dots suffer from (i) limited spectral coverage of the solar spectrum (usually working mainly in the ultraviolet-blue region, with typically a 300–500 nm absorption band) and (ii) low QYs because of the existence of abundant structural and surface defects, which lead to external optical efficiency lower than that of inorganic heavy-metal-containing QD based LSCs (2–4% with dimensions of 10×10 cm^2).[9,34–37] Moreover, the photo/thermal stability of LSCs is still an open issue that prevents their practical applications.

In this work, we demonstrated a highly efficient large-scale LSC using red-emissive C-dots. The red-emissive C-dots exhibit a broad ultraviolet-visible spectrum absorption (300–600 nm), long-wavelength emission (550–700 nm), high QY (~65%) and large Stokes shift (~ 0.45 eV). Transient absorption measurements performed with high temporal resolution (~150 fs) revealed the ultrafast formation of the broad emissive state, which takes place in about 1 ps. The LSC was prepared by embedded C-dots in polymethyl methacrylate (PMMA) on a glass substrate. The large-area LSC ($10 \times 10 \times 0.52$ cm^3) exhibits an optimal external optical efficiency of 4.81% and a PCE of 2.41% under natural sun irradiation (70 mW cm^{-2}) after coupling to silicon solar cells. Moreover, a tandem LSC using green-emissive C-dots and red-emissive C-dots (top and bottom layers correspondingly) as fluorophores exhibited an external optical efficiency as high as 6.78%.

Experimental section

Synthesis of C-dots

The red-emissive C-dots were synthesized using a solvothermal method based on nitrated pyrenes and functionalized with boric acid (H_3BO_3).[38] Firstly, pyrene was nitrated by mixing 2 g pyrene and 240 mL HNO_3 (16 M) under 150 rpm stirring at 80 °C for 24 h. After the reaction was stopped, 2 L distilled water was added and stirred at room temperature for 24 h. Then the nitrated pyrenes were collected after filtering and drying. Secondly, the solvothermal method was used to produce C-dots: 2 g nitrated pyrenes and 1 g boric acid (H_3BO_3) mixed with 50 mL dimethylformamide (DMF) solvent were stirred and ultrasonicated for 0.5 h. Then the mixture was transferred to an autoclave for the solvothermal reaction at 180 °C for 12 h. Finally, the as-synthesized C-dots were collected by high-speed centrifugation and redispersed in toluene for further characterization and used in fabricating LSCs.

Green-emissive C-dots were prepared using a space-confined vacuum-heating approach.[31] Typically, 1 g citric acid, 2 g urea and 1 g $CaCl_2$ were mixed with 2 mL water under stirring until the aqueous solution was clear. Then the mixture was heated to 120 °C under vacuum for 30 min to pump away the water and then gradually heated to 180 °C for 30 min and then to 250 °C for 1 h. Finally, the product was dispersed in methanol and centrifuged at 8000 rpm for 10 min. The supernatant was transferred into dialysis bags with a molecular weight of 300 Da for 12 h and then the C-dots/methanol solution inside the dialysis bag was collected and dried. The C-dots were redispersed in methanol for further application in LSCs.

LSC fabrication

A film structured LSC was fabricated by a drop-casting approach. In detail, 10 mL red-emissive C-dots dispersed in toluene, containing 1.2–1.5 mg C-dots, were mixed with 2 g polymethyl methacrylate (PMMA). The mixture was stirred for 12 h to obtain a clear mixture, which was drop-cast on the surface of a glassy substrate ($5 \times 5 \times 0.5$ cm^3 and $10 \times 10 \times 0.5$ cm^3) and dried at room temperature for 3 h until all the solvent was evaporated. The volume of the QDs/polymer solution cast on the substrate is 10 mL and 2.5 mL for the substrate with a size of $10 \times 10 \times 0.5$ cm^3 and $5 \times 5 \times 0.5$ cm^3, respectively. The thickness of the LSC active layer is about 0.17 ± 0.02 mm measured by using a thickness gauge meter CHY-C2A. For the green-emissive C-dot based LSCs, a 10 mL green-emissive C-dot methanol mixture, containing 10–20 mg C-dots, 2 g polyvinyl pyrrolidone (PVP) K30, and 1 g PVP K90, was obtained, and then the same procedures as for the preparation of red-emissive C-dot based LSCs was followed.

Characterization

Transmission electron microscopy (TEM) and high-resolution TEM (HRTEM) measurements were carried out using a JEOL JEM 2100Plus TEM operating at 200 kV. X-ray photoelectron spectroscopy (XPS) spectra were recorded using a Thermo Scientific K-Alpha XPS spectrometer. Fourier transform infrared (FT-IR) spectroscopy was carried out by using a Thermo Fisher Scientific Nicolet iS5 FT-IR spectrometer. Absorption spectra were recorded using a TU-1901 double beam UV-Vis spectrophotometer. Photoluminescence (PL) spectra were collected by using a Cary Eclipse fluorescence spectrophotometer with an

This journal is © The Royal Society of Chemistry 2023

J. Mater. Chem. A, 2023, 11, 8950–8960 | 8951

excitation wavelength of 365 nm. Transient PL spectra were recorded on an Edinburgh FLS980 fluorescence spectropho-tometer. QY was recorded with an Edinburgh FLS1000 spec-trofluorimeter equipped with an integrating sphere. Femtosecond transient absorption measurements (fs-TA) were performed using a Helios fs-TA spectrometer (Ultrafast Systems, USA).

Excitation-distance dependence PL spectra were collected by fixing the position of one LSC edge facing the detector and exciting the LSC with a movable laser ($\lambda_{ex} = 365$ nm) perpendicular to the top surface of the LSC. The spot size of the exciting light was ~0.75 mm^2. The external optical efficiency of the LSCs was measured under standard solar illumination using a solar simulator (Newport) at AM 1.5G (100 mW cm^{-2}) or under natural sunlight illumination. In order to irradiate the full area of the LSCs, for the LSC with a size of $5 \times 5 \times 0.52$ cm^3, the measurement was performed under a solar simulator; meanwhile for the LSC with a size of $10 \times 10 \times 0.52$ cm^3, the measurement was carried out under natural sunlight illumination. During measurements, the solar cell was directly coupled on one side of LSC edges. The application of anti-reflection coatings and plasmonic and back-reflector design strategies to overcome the photon energy loss in solar cells have been reported in previous reports.[39,40] In the LSC-PV system, to avoid the inevitable loss of energy caused by coupling the solar cell to the LSC, we used a transparent epoxy to connect the solar cell with the LSC, which can decrease the reflections caused by the different refractive index between the solar cell surface and air. In the calculation of the efficiency, we estimated the total power produced by the LSC as the power produced from one side multiplied by four (for a square LSC). To validate this procedure, we measured the produced power under the same irradiation conditions at different sides of the LSC and we found no discrepancy, within the measurement uncertainty, in the measured power values from different LSC sides. To avoid any reflection from the three sides, where no PV cell is placed, we masked them with black tape, able to completely absorb the radiation from the LSC. This way, we minimize possible over-estimation of PCE coming from either reflected light or light entering the lateral sides of the LSC, where no PV cell is placed. The current–voltage (J–V) characteristics were measured by using a Keithley 2400 Source Meter. Through measuring the changes of solar cell current after direct solar irradiation and LSC irradiation, the external optical efficiency (η_{opt}) can be defined as:[36]

$$\eta_{opt} = \frac{J_{LSCs}}{J_{SC} \times G} \qquad (1)$$

where J_{LSCs} and J_{SC} are the short circuit current density from the solar cell coupled with the LSCs and from the same solar cell under direct sunlight illumination. G is the geometric factor, defined as a ratio between the area of the top surface and that of the edges of the LSC ($G = A_{surface}/A_{edges}$). For all the measurements, three LSCs were fabricated using the same procedure and the average optical efficiency was obtained for three sets of measurements under similar light intensity. During efficiency measurements at different temperatures, we used a heating

plate to increase the temperature and used a hand-held infrared thermometer to monitor the temperature change. The efficiency test in the cooling process adopts the natural cooling method to test the efficiency change at different temperatures when the temperature drops to room temperature. Specifically, in the positive temperature range from room temperature to 60 °C, we used a heating plate to control the temperature, and we recor-ded the J–V curves of the solar cell and LSC-solar cell system to evaluate the efficiency of the device. For the negative tempera-ture range, we used the change of PL spectra to evaluate the change of the efficiency. The temperature was controlled with liquid nitrogen, and the PL spectra were recorded *in situ* by using an Edinburgh FLS980 fluorescence spectrophotometer.

For the stability study of the LSCs under different wavelength irradiation, we selected three kinds of filters (350 ± 5 nm, 450 ± 5 nm, and 550 ± 5 nm) to filter the sunlight irradiated on the LSCs, and compared them with the LSC without filters and the LSC in a dark environment to study the efficiency variation of the LSCs ($5 \times 5 \times 0.52$ cm^3) under different wavelengths of sunlight irradiation as a function of irradiation time. The optical efficiency measurements were carried out under solar simulator illumination. For the long-time stability study of the LSCs, we used a large-area LSC ($10 \times 10 \times 0.52$ cm^3) as an example, and put it in a natural room for 2 months (ambient atmosphere, humidity of 40–60%, day and night, and without any light filter). Then the J–V curve of the LSC-solar cell system under outdoor natural sunlight illumination was obtained and eqn (1) was used to calculate the external optical efficiency of the LSC.

Results and discussion

The C-dots were prepared by a solvothermal approach with surface functionalization based on small aromatic molecules and boric acid. TEM characterization reveals the morphology and microstructure of the as-synthesized C-dots, as shown in Fig. 1. From the TEM image, it can be seen that the C-dots have a typical spherical shape and the average size is ~2.88 nm with highly uniform dispersion (Fig. 1a and b). The HRTEM image of one individual nanoparticle (Fig. 1c) reveals that the C-dot has a diamond cubic crystalline structure. The two planes with a lattice spacing of 2.05 Å and 1.87 Å correspond to the (2$\bar{1}$0) and (211) planes of diamond cubic carbon. The full survey of XPS is shown in Fig. S1a,† demonstrating that the main elements of C, O, N, and B existed in C-dots. The high-resolution spectrum of C 1s and O 1s can be divided into two peaks, corresponding to different bonds (C–C, C–O, and O–H). A single dominant peak appeared in the B 1s spectrum, proving the boric acid func-tionalization. The FT-IR spectrum of the C-dots (Fig. S2a†) shows strong and broad stretching vibrations at 3648–3270 cm^{-1}, corresponding to the presence of O–H and N–H. The peaks at 2961, 2923 and 2851 cm^{-1} could be ascribed to C–H stretching vibrations. The peaks located at 1602 and 1506 cm^{-1} can be attributed to the stretching vibration of the aromatic ring skeleton (C=C). Moreover, the peak at 1261 cm^{-1} can be attributed to the C–O stretching vibration on the aromatic ring. The bands at 1096 and 1023 cm^{-1} reflect the stretching

8952 | *J. Mater. Chem. A*, 2023, **11**, 8950–8960

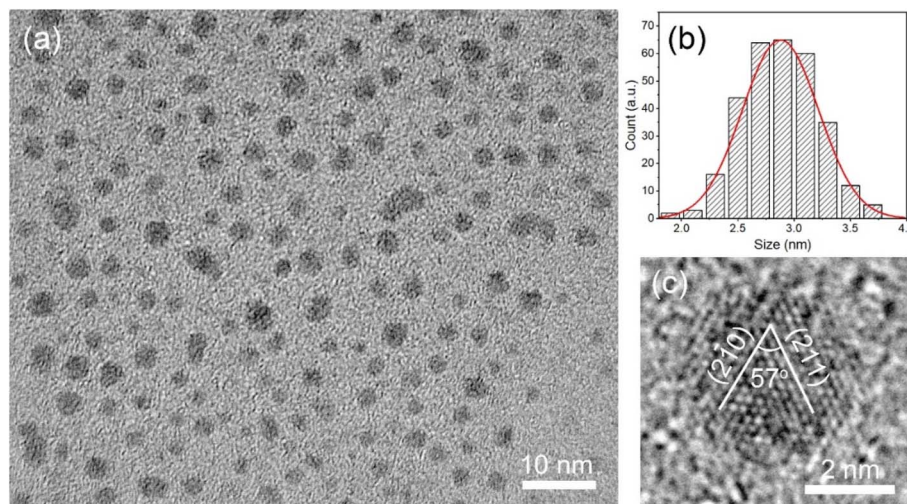This journal is © The Royal Society of Chemistry 2023

Fig. 1 (a) TEM image and (b) size distribution of red-emissive C-dots. (c) HRTEM image of one red-emissive C-dot.

vibration of the C–N group. The C–O, C–H, O–H and N–H stretching vibrations observed by FT-IR confirm the presence of the carboxyl, amide and hydroxyl groups on the surface of the C-dots.[41–43] Based on the above structural characterization, the diagram in Fig. S2b† illustrates the structure and surface groups of the C-dots.

Fig. 2a shows the ultraviolet-visible (UV-vis) absorption and normalized PL spectra of the C-dots dispersed in toluene. It shows that the C-dots have a broad absorption spectrum (from the ultraviolet to visible range, with onset at 600 nm and the first-excitonic absorption peak at 490 nm) and red emission ranging from 550 nm to 700 nm with a peak located at ~595 nm, which means that they have a large Stokes shift of 0.45 eV. The PL decay curve of the C-dots in toluene is shown in Fig. 2b, which can be fitted by a single-exponential decay curve with a PL lifetime of 8.6 ns. The QY of the C-dots was obtained by means of an integrating sphere (λ_{ex} = 500 nm) coupled to a PL spectrometer. For the absolute QY measurement, the excitation and
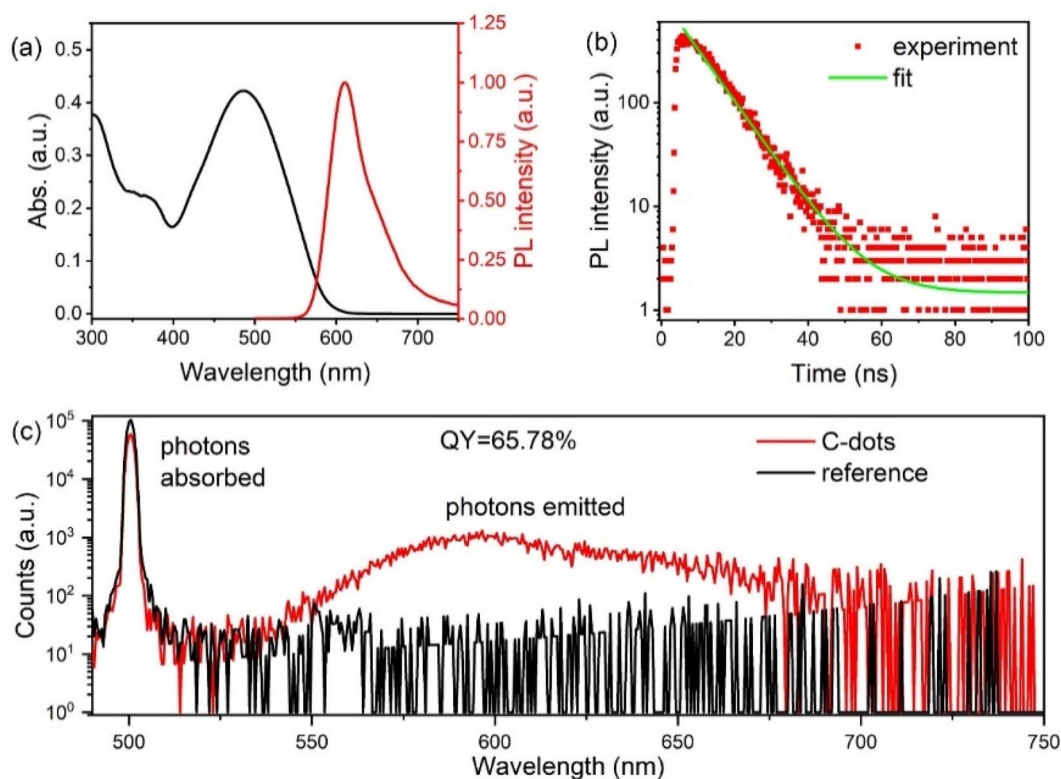

Fig. 2 (a) UV-vis absorption and PL spectra of the C-dots dispersed in toluene. (b) PL decay curve of the C-dots excited at λ_{ex} = 375 nm and an emission wavelength of 600 nm. (c) Experimental raw data of the absolute QY measurement of the C-dots in toluene.

This journal is © The Royal Society of Chemistry 2023

J. Mater. Chem. A, 2023, 11, 8950–8960 | 8953

emission of both the QD sample and reference (background without QDs, see the black line in Fig. 2c) were measured to compare. By comparing the differences in the sample and reference data, the excitation (494.0–506.5 nm) and emission (527.0–732.0 nm) spectra can be divided, and thus the number of photons absorbed and emitted can be derived (Fig. 2c), which shows that the C-dots have a high QY of ~66% in toluene, mainly driven by the development of highly brilliant luminophores. Using the QY and PL lifetime, we can calculate the radiative and nonradiative decay rates of the C-dots. The QY can be expressed as:

$$QY = \frac{k_r}{k_r + k_{nr}} \qquad (2)$$

The lifetime can be calculated as:

$$\tau = \frac{1}{k_r + k_{nr}} \qquad (3)$$

where k_r and k_{nr} are the radiative and nonradiative decay rates, respectively. The calculated k_{nr} and k_r were 3.9×10^{-2} ns^{-1} and 7.6×10^{-2} ns^{-1}, respectively, indicating a dominate radiative recombination mechanism. Both the high QY and single-

exponential decay behavior point to efficient radiative recombination processes in the red-emissive C-dots.

To further explore the exciton dynamics of the red-emissive C-dots, fs-TA spectroscopy measurements were carried out by the pump-probe technique, under excitation at 365 nm and using a broad visible probe, with a temporal resolution of about 150 fs. The collected data are shown in Fig. 3. Fig. 3a displays the contour plot, for the 430–720 nm probe spectral range, and time delays up to 1000 ps. The two positive bands, peaked at around 490 nm and 700 nm, represent photo-induced absorption processes and can be assigned to excited state absorption (ESA); its evolution describes the excited state population. The broad negative signal, peaked at ~594 nm and extending roughly from 570 and 670 nm, spectrally coincides with PL and thus accounts for stimulated emission (SE). Fig. 3b and c display TA spectra at different time delays and TA kinetics at selected wavelengths, respectively. It can be noted that the excited state is populated in about 600 fs and reach its maximum population in ~1 ps (see Fig. 3c). ESA has a very broad band, which covers all the probed region, from 430 nm to 720 nm, as can be seen in the plot of Fig. 3b (light pink line in Fig. 3b, at 0.5 ps time delay). In the spectral region around 594 nm we observe a competition between ESA and SE. Initially
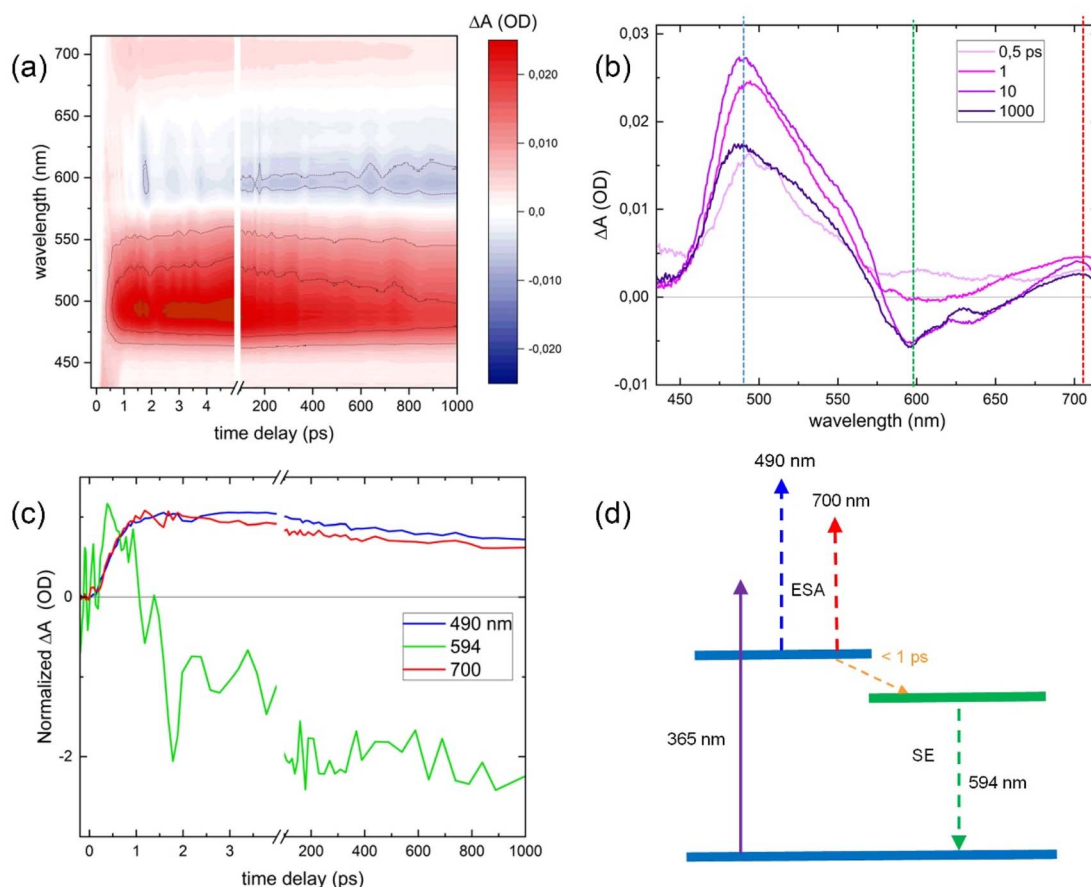

Fig. 3 fs-TA ultrafast pump-probe measurements of red-emissive C-dots in toluene with a pump wavelength at 365 nm; (a) 2D map; (b) TA spectra at indicated delay times (from 0.5 to 1000 ps); (c) TA kinetics at selected wavelengths (indicated also in panel b). (d) Scheme of the electronic band structure and of the population dynamics.

8954 | J. Mater. Chem. A, 2023, 11, 8950–8960

This journal is © The Royal Society of Chemistry 2023

ESA is stronger than SE, but in ~1 ps SE overcomes ESA, and, correspondingly, the TA signal changes sign: from positive to negative (see the green line in Fig. 3c). This shows the evolution of the emissive state: the formation of the broad emissive state is ultrafast, it is stronger than any other absorption mechanism and its fast formation outcompetes any other form of relaxation. This is consistent with the hypothesis of a single, well-defined de-excitation channel.

On longer time delays, we observed some rearrangements in the first 4–5 ps, and similar evolution for all bands on longer time scales (up to 1 ns at least). In particular, two bands of ESA (around 490 and 700 nm) show the same decay (Fig. 3c), and this confirms the assignment of both ESA to the same starting state. The SE band, at 594, shows a very slow decay, with a lifetime exceeding 1 ns, which is consistent with PL evolution. In Fig. 3d we depicted a scheme of the band structure and of the population evolution of the red-emissive C-dots.

The above excellent optical properties, especially the wide absorption, fast and stable PL emission and high QY, make the red-emissive C-dots a potential fluorescent material for efficient LSCs. The LSCs were obtained by mixing the C-dots (synthesized by a solvothermal reaction) with PMMA polymer/toluene and by drop-casting on glass substrates (details in the Experimental section). We further detached the QDs/PMMA from the glass and measured the thickness of the as-prepared film using a CHY-C2A thickness system for selecting 100 points in the film (Fig. S3a†). Fig. S3b† shows that the thickness of the film ranges from 143 to 222 μm, with the main thickness distribution range of ~150–190 μm, indicating the uniformity of the film. Fig. 4a

shows a typical LSC with the dimensions of $10 \times 10 \times 0.52$ cm^3 ($G = 4.84$) under simulated solar irradiation. It clearly shows that the as-prepared LSC was semi-transparent and a clear concentrated red light could be propagated to the edges of the LSC. There was no significant difference in the absorption and emission spectra for the C-dots dispersed in toluene and in the PMMA polymer film (Fig. 4b and c). A slight peak position variation of the C-dots in the LSC was most probably due to the change in the refractive index of the matrix (toluene solution *vs.* PMMA polymer). As shown in Fig. S4,† the C-dots dispersed in toluene, hexane and water exhibit different emission colors due to the different refractive index. The PL lifetime of the C-dots in the PMMA film was ~8.2 ns, showing a very slight difference compared with the C-dots dispersed in toluene (Fig. 4d). The QY of the C-dots in the LSC also shows a slight decrease compared with that in toluene due to the effect of the medium (for example the defects in the polymer lead to fluorescence quenching), but it still maintained ~50% under 500 nm excitation (Fig. 4e), indicating potential for BIPVs.

Following a method reported in the literature,[30] we performed distance-dependent PL measurements to evaluate the distance dependence of the efficiency, as shown in Fig. 5a. Fig. 5b shows the change of total PL intensity with increasing the distance of the irradiation from the side edge. The inset in Fig. 5b illustrates the measurement process of the distance-dependent PL. For the LSC with the dimensions of $10 \times 10 \times 0.52$ cm^3, the PL intensity of the C-dots decreased with the increase of the distance between the beam spot and edge of the LSC. When the beam spot irradiated in the central region of the
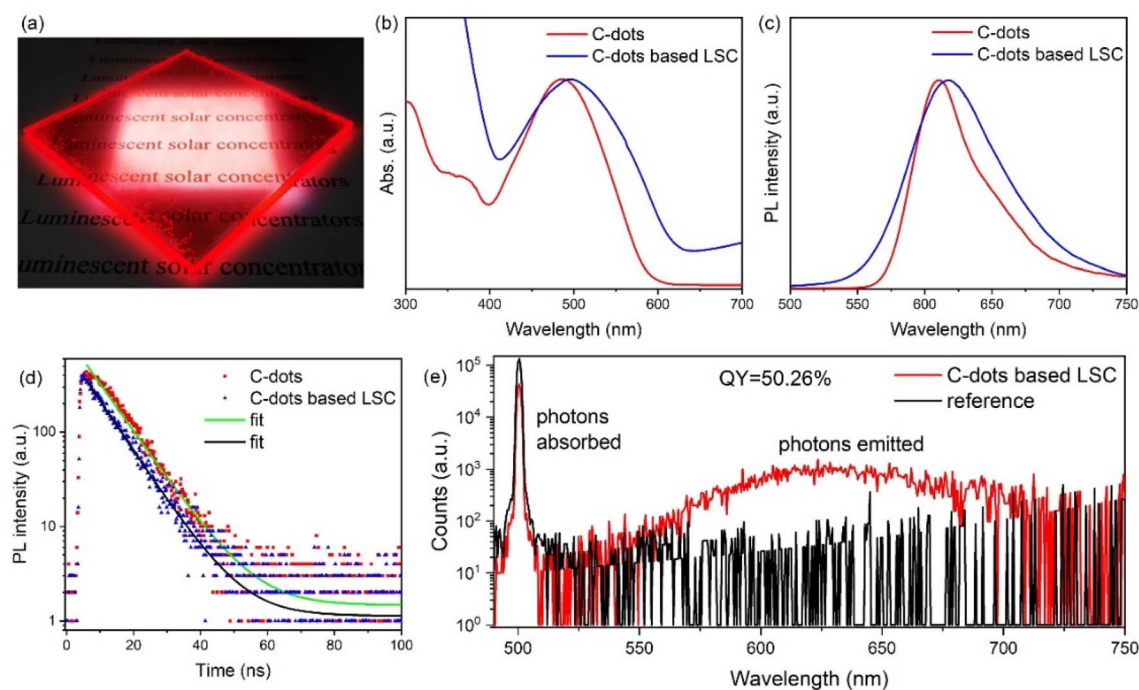

Fig. 4 (a) Photograph of the red-emissive C-dot based LSC. (b) Absorption, (c) PL emission spectra with the same excitation wavelength of 365 nm and (d) PL decay curves of the C-dots in toluene and PMMA polymer. (e) The numbers of photons absorbed and emitted in the QY measurement of the C-dots in the LSC.
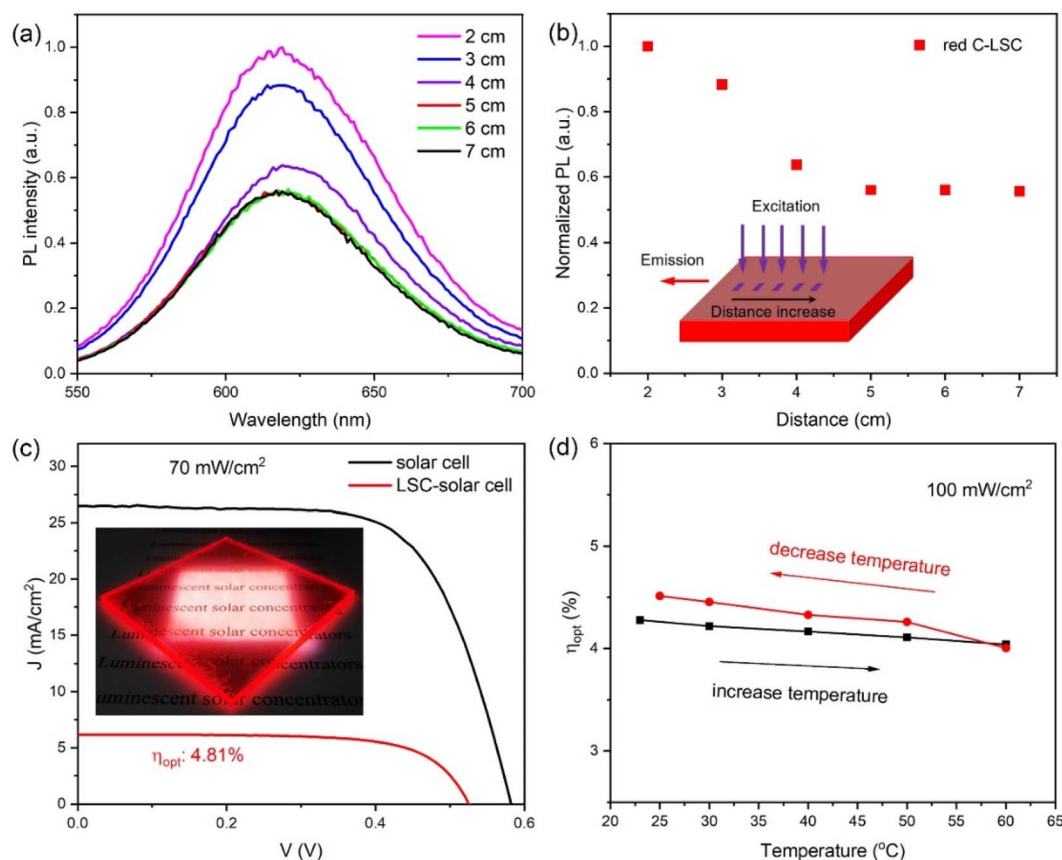
This journal is © The Royal Society of Chemistry 2023

J. Mater. Chem. A, 2023, **11**, 8950–8960 | **8955**

Fig. 5 Red-emissive C-dot LSC (a) PL intensity spectra for different distances of irradiation from the edge. (b) Total PL intensity (integral over the spectrum) as a function of the distance of the irradiation from the side edge. Inset shows the schematic of the measurement. (c) J–V curve of the LSC-solar cell system upon natural sunlight illumination (~70 mW cm^{-2}). Inset shows the photograph of the LSC ($10 \times 10 \times 0.52$ cm^3) under a solar simulator. (d) The variations of the external optical efficiency of the LSC with temperature changes.

LSC (5–7 cm away from the edge of the LSC), the PL intensity of the device maintains a nearly stable value. This means that the optical efficiency of the LSC decreased with the increase of the light propagation distance due to the reabsorption and G. This phenomenon has been widely reported and used to evaluate the reabsorption loss in LSCs.[27,30,44] In our case, the reabsorption is very low, as verified by Fig. 5a, where the shape of PL is almost unaffected, meaning that very weak resorption is present. In generally, in addition to the reabsorption loss due to the re-absorption and re-emission, the energy loss in an LSC is also affected by the following aspects: transmitted light (non-absorption of incident photons), partial light loss due to non-unity of the QY (<100%), surface reflection and the escaped light below the critical angle. To further understand the distance-dependent efficiency of the LSCs, the external optical efficiency (η_{opt}) of the LSCs was calculated. The theoretical optical efficiency of the LSCs is defined as the edge emitted photons over the total incident photons. It can be calculated as:[45]

$$\eta_{\text{opt}} = \eta_{\text{abs}} \times \eta_{\text{internal}} \tag{4}$$

where η_{abs} is the absorbed sunlight by the LSCs and the η_{internal} is the internal quantum efficiency of the LSC. The η_{abs} of the LSC can be calculated as:[45]

$$\eta_{\text{abs}} = (1 - R)\frac{\int_0^\infty I_{\text{in}}(\lambda)\left(1 - \mathrm{e}^{-\alpha(\lambda)d}\right)\mathrm{d}\lambda}{\int_0^\infty I_{\text{in}}(\lambda)\mathrm{d}\lambda} \tag{5}$$

where $I_{\text{in}}(\lambda)$ is the solar irradiation, $\alpha(\lambda)$ is the absorption coefficient $\alpha(\lambda) = \ln(10)\dfrac{A(\lambda)}{d}$, in which $A(\lambda)$ is the absorption of the LSC, and d is the thickness of the LSC. R is the reflection coefficient, which is associated with the refractive index of the LSC. The η_{internal} of the LSC can be expressed as:[45]

$$\eta_{\text{internal}} = \frac{\int_0^\infty \dfrac{\eta_{\text{QY}}\eta_{\text{trap}}}{1 + \beta\alpha(\lambda)L\left(1 - \eta_{\text{QY}}\eta_{\text{trap}}\right)}I_{\text{PL}}(\lambda)\mathrm{d}\lambda}{\int_0^\infty I_{\text{PL}}(\lambda)\mathrm{d}\lambda} \tag{6}$$

where η_{QY} is the QY of the QDs in LSCs, I_{PL} is the measured PL emission spectrum, β factor is a numerical value fixed to 1.4 as reported by Klimov *et al.*,[45] L is the length of the LSC, and η_{trap} is the efficiency of light trapping into the LSC.

The calculated external optical efficiency of the LSCs is shown in Fig. S5.† In the simulation, the sunlight absorbed by

8956 | *J. Mater. Chem. A*, 2023, **11**, 8950–8960

This journal is © The Royal Society of Chemistry 2023

the LSC was ~15.3% of the total solar spectral energy (Fig. S5a†) and the QY of the C-dots was set to 65%. As shown in Fig. S5b,† the optical efficiency shows a decrease with the increasing length of the LSC. We further measured the optical efficiency of the LSC by coupling a solar cell at the edge of the LSC (details in the Experimental section). In the case of large-area LSCs ($10 \times 10 \times 0.52$ cm^3), the power intensity was 70–80 mW cm^{-2}, which was determined by the natural sunlight irradiation (Qingdao, China). In the case of the small-area LSCs ($5 \times 5 \times 0.52$ cm^3), the power intensity was set at 100 mW cm^{-2} (AM 1.5G standard) using a calibrated solar simulator. The measured optical efficiency of the LSCs was $4.5 \pm 0.3\%$ ($10 \times 10 \times 0.52$ cm^3) and $4.8 \pm 0.2\%$ ($5 \times 5 \times 0.52$ cm^3). Although the experimental result is systematically lower than the calculated optical efficiency due to the scattering of the surface or lower absorption, the variation trend of efficiency with size is consistent with the theoretical results (Fig. S5b†). As shown in Fig. 5c, the optimal optical efficiency of the LSCs ($10 \times 10 \times 0.52$ cm^3) was measured to be 4.81% under natural sunlight illumination (70 mW cm^{-2}). This is the highest efficiency of LSCs based on C-dots,[34,35,46–49] compatible with the 75% trap efficiency,[50] thanks to their large absorption range, high QY and large Stokes shift. To understand the actual contribution of the C-dots to the optical efficiency, we further tested the J–V curve of the PMMA film/glass-

solar cell system without luminophores, as shown in Fig. S6.† The result indicates that 98% of the optical efficiency of the LSC is contributed by the C-dots. A comparative analysis of the performance of LSCs based on different types of C-dots is also reported in Table S1 in the ESI.† The LSC-Si solar cell configuration exhibits a PCE of 2.41% under natural sunlight (70 mW cm^{-2}), which is larger than most of the reported C-dot based LSCs[30,38,46,51] and comparable to doped-C-dot based LSCs.[52]

LSCs are supposed to be used outdoors under various conditions, and the thermal stability plays an important role in the LSC system. Furthermore, the temperature dependence of the efficiency was measured, as shown in Fig. 5d. It can be seen that when the temperature increased from room temperature to 60 °C, the η_{opt} gradually decreased. When the temperature further decreased to room temperature, the efficiency increased. The thermal stability of the as-fabricated LSCs maintained 89% of its original value even at a high temperature of 60 °C, which is comparable to previous reports (Table S2†). We used negative temperatures to characterize the efficiencies over a wide temperature range (Fig. S7†). The results show that the integrated PL intensity can maintain 77% of its highest value at −50 °C. Considering that the PL intensity determines the optical efficiency of the LSC, we used the variation of PL spectra to evaluate the change of the efficiency in the negative
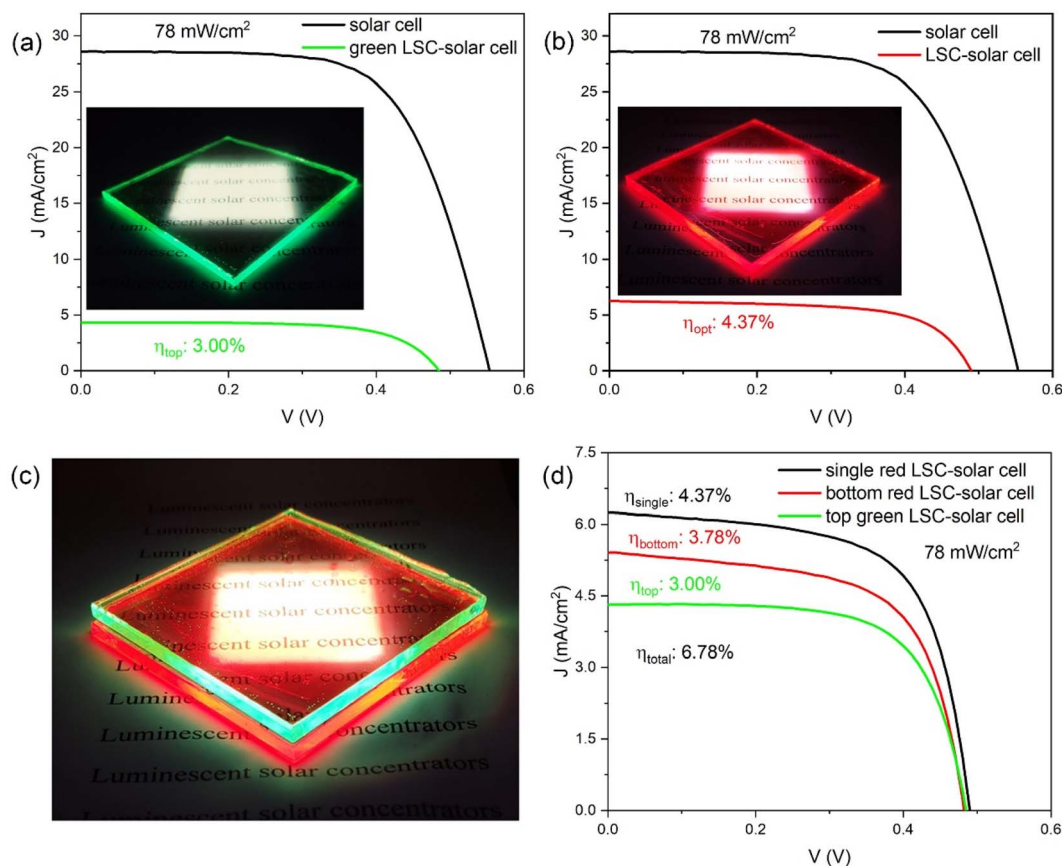

Fig. 6 (a and b) J–V curves of the green C-dot based LSC (a) and red C-dot based LSC (b) coupled with solar cells under natural sunlight irradiation (78 mW cm^{-2}). Insets show the photograph of the LSC. (c) Photograph of the tandem structured LSC. (d) J–V curves of the single layered red C-dot based LSC and the tandem structured LSC coupled with solar cells under natural sunlight irradiation (78 mW cm^{-2}).

This journal is © The Royal Society of Chemistry 2023

J. Mater. Chem. A, 2023, **11**, 8950–8960 | **8957**

temperature range. It can be seen that the PL peak position shows no obvious changes while the PL intensity increased and then decreased when the temperature increased from −30 °C to 50 °C. This means that the efficiency also increases first and then decreases as the temperature rises from −30 °C to 50 °C. When the temperature is set at 0 °C, the PL intensity is the highest, which indicates that LSCs have the highest efficiency when the temperature is 0 °C. All the results demonstrate the outstanding thermal stability of the C-dot based LSCs.

To further improve the optical efficiency of the LSC, a tandem structure was designed based on C-dots as fluorescent materials. In this structure, green-emissive fluorescent C-dots were embedded in PVP to prepare a green-emissive LSC film (details in the Experimental section). Fig. S8† shows that this kind of C-dots in methanol have an absorption spectrum covering the 300–460 nm range. After excitation at 365 nm, the C-dots exhibit a broad PL emission in the 450–650 nm range with a peak located at ∼520 nm. Their lifetime is 16.2 ns longer than that of the above red-emissive C-dots (8.6 ns). Similar to red-emissive C-dots, after the green-emissive C-dots are embedded into the PVP polymer, the absorption, PL emission spectra and PL decay curves also show a slight difference due to the change of the refractive index of the surrounding (Fig. S8†). Furthermore, following the same measurement method, we performed distance-dependent PL measurements as shown in Fig. S9.† For the green-emissive LSC ($10 \times 10 \times 0.52$ cm³), the PL intensity of the C-dots decreased with the increase of the distance between the irradiation beam spot and edge of the LSC, which is similar to the red-emissive LSCs due to the reabsorption energy loss and G.

The optical efficiency of the green-emissive C-dot based LSC is 3.00% under the irradiation of natural sunlight (78 mW cm⁻²), as shown in Fig. 6a. Under the same operation conditions, the red-emissive C-dot based LSC exhibits an external optical efficiency of 4.37% ($10 \times 10 \times 0.52$ cm³) (Fig. 6b). For the tandem structure, the green-emissive C-dot based LSC was placed at the top of the red-emissive C-dot based LSC, as shown in Fig. 6c. In this structure, the optical efficiency of the green LSC is still maintained at 3.00%, while the efficiency of the red LSC is decreased from 4.37% to 3.78% (Fig. 6d), due to the absorption of the top layer. Thus, the total optical efficiency of the tandem structure is 6.78%, which is the highest ever reported efficiency among all the different configurations and types of C-dot based LSCs.[34,35,46–49]

To investigate the long-term stability of the C-dot based LSCs, we measured the external optical efficiency variation of the LSCs ($5 \times 5 \times 0.52$ cm³) upon different sunlight illumination (350 ± 5 nm, 450 ± 5 nm, 550 ± 5 nm, full solar spectrum and dark) under natural conditions (Fig. S10†). The results show that the UV and visible light in the absorption range of the C-dots can both lead to the decrease of the optical efficiency. Under the same conditions, when there is no light irradiation, the efficiency of the LSCs also decreases, especially when the air humidity is high (>80%). This means that both sunlight and moisture can influence the properties of the LSCs. When the LSC ($10 \times 10 \times 0.52$ cm³) was placed in a natural room for 2 months, the efficiency decreased to 3.46% (Fig. S11†), keeping

72% of its initial value, indicating a good stability of the device. Further to improve the stability, encapsulating the device with epoxy glue or a laminated structure can be used to isolate the C-dots from the external environments (air, moisture or other chemicals).

Conclusions

In conclusion, we demonstrated large-area and highly efficient LSCs based on red-emissive C-dots. These C-dots possess a broad absorption range of 300–600 nm, high QY of ∼65% and large Stokes shift of ∼0.45 eV. These features make the C-dots suitable as a promising fluorophore for highly efficient LSCs. Large-area LSCs ($10 \times 10 \times 0.52$ cm³) based on these C-dots exhibit a record external optical efficiency of 4.81%, and after coupling to silicon solar cells, they show a PCE of 2.41% under natural sunlight illumination (70 mW cm⁻²). By placing a green-emissive C-dot based LSC on the top of the LSC to form a tandem structure, the external optical efficiency was improved up to 6.78%. After placing the LSC under natural indoor irradiation for 2 months, the efficiency maintained 72% of its initial value. These findings demonstrate that the eco-friendly carbon-based nanomaterials are promising luminescent materials for highly efficient large-area LSCs.

Conflicts of interest

There are no conflicts to declare.

Acknowledgements

References

1 L. Meng, J. You and Y. Yang, Addressing the stability issue of perovskite solar cells for commercial applications, *Nat. Commun.*, 2018, **9**, 5265.

2 Y. Rong, Y. Hu, A. Mei, H. Tan, M. I. Saidaminov, S. I. Seok, M. D. McGehee, E. H. Sargent and H. Han, Challenges for commercializing perovskite solar cells, *Science*, 2018, **361**, eaat8235.

3 G. S. Selopal, H. G. Zhao, G. J. Liu, H. Zhang, X. Tong, K. H. Wang, J. Tang, S. H. Sun, S. H. Sun, F. Vidal, Y. Q. Wang, Z. M. Wang and F. Rosei, Interfacial engineering in colloidal "giant" quantum dots for high performance photovoltaics, *Nano Energy*, 2019, **55**, 377–388.

8958 | *J. Mater. Chem. A*, 2023, **11**, 8950–8960

This journal is © The Royal Society of Chemistry 2023

4 H. Hernandez-Noyola, D. H. Potterveld, R. J. Holt and S. B. Darling, Optimizing luminescent solar concentrator design, *Energy Environ. Sci.*, 2012, **5**, 5798–5802.

5 F. Mateen, M. A. Saeed, J. W. Shim and S. K. Hong, Indoor/outdoor light-harvesting by coupling low-cost organic solar cell with a luminescent solar concentrator, *Sol. Energy*, 2020, **207**, 379–387.

6 M. J. Currie, J. K. Mapel, T. D. Heidel, S. Goffri and M. A. Baldo, High-efficiency organic solar concentrators for photovoltaics, *Science*, 2008, **321**, 226–228.

7 M. G. Debije, R. C. Evans and G. Griffini, Laboratory protocols for measuring and reporting the performance of luminescent solar concentrators, *Energy Environ. Sci.*, 2021, **14**, 293–301.

8 R. Mazzaro and A. Vomiero, The renaissance of luminescent solar concentrators: The role of inorganic nanomaterials, *Adv. Energy Mater.*, 2018, **8**, 1801903.

9 K. Wu, H. Li and V. I. Klimov, Tandem luminescent solar concentrators based on engineered quantum dots, *Nat. Photonics*, 2018, **12**, 105–110.

10 M. R. Bergren, N. S. Makarov, K. Ramasamy, A. Jackson, R. Guglielmetti and H. McDaniel, High-performance $CuInS_2$ quantum dot laminated glass luminescent solar concentrators for windows, *ACS Energy Lett.*, 2018, **3**, 520–525.

11 F. Meinardi, F. Bruni and S. Brovelli, Luminescent solar concentrators for building-integrated photovoltaics, *Nat. Rev. Mater.*, 2017, **2**, 17072.

12 C. A. C. Chazot, S. Nagelbert, C. J. Rowlands, M. R. J. Scherer, I. Coropceanu, K. Broderick, Y. Kim, M. G. Bawendi, P. T. C. So and M. Kolle, Luminescent surfaces with tailored angular emission for compact dark-field imaging devices, *Nat. Photonics*, 2020, **14**, 310–315.

13 F. Zhao, D. Cambie, J. Janse, E. W. Wieland, K. P. L. Kuijpers, V. Hessel, M. G. Debije and T. Noel, Scale-up of a luminescent solar concentrator-based photomicroreactor via numbering-up, *ACS Sustainable Chem. Eng.*, 2018, **6**, 422–429.

14 S. M. El-Bashir, F. F. Al-Harbi, H. Elburaih, F. Al-Faifi and I. S. Yahia, Red photoluminescent PMMA nanohybrid films for modifying the spectral distribution of solar radiation inside greenhouses, *Renewable Energy*, 2016, **85**, 928–938.

15 M. Portnoi, P. A. Haigh, T. J. Macdonald, F. Ambroz, I. P. Parkin, I. Darwazeh and I. Papakonstantinou, Bandwidth limits of luminescent solar concentrators as detectors in free-space optical communication systems, *Light: Sci. Appl.*, 2021, **10**, 3.

16 Y. Zhou, H. Zhao, D. Ma and F. Rosei, Harnessing the properties of colloidal quantum dots in luminescent solar concentrators, *Chem. Soc. Rev.*, 2018, **47**, 5866–5890.

17 F. Meinardi, A. Colombo, K. A. Velizhanin, R. Simonutti, M. Lorenzon, L. Beverina, R. Viswanatha, V. I. Klimov and S. Brovelli, Large-area luminescent solar concentrators based on 'Stokes-shift-engineered' nanocrystals in a mass-polymerized PMMA matrix, *Nat. Photonics*, 2014, **8**, 392–399.

18 A. Anand, M. L. Zaffalon, G. Gariano, A. Camellini, M. Gandini, R. Brescia, C. Capitani, F. Bruni, V. Pinchetti, M. Zavelani-Rossi, F. Meinardi, S. A. Crooker and S. Brovelli, Evidence for the band-edge exciton of $CuInS_2$ nanocrystals enables record efficient large-area luminescent solar concentrators, *Adv. Funct. Mater.*, 2020, **30**, 1906629.

19 H. C. Bauser, C. R. Bukowsky, M. Phelan, W. Weigand, D. R. Needell, Z. C. Holman and H. A. Atwater, Photonic crystal waveguides for >90% light trapping efficiency in luminescent solar concentrators, *ACS Photonics*, 2020, **7**, 2122–2131.

20 F. Meinardi, S. Ehrenberg, L. Dhamo, F. Carulli, M. Mauri, F. Bruni, R. Simonutti, U. Kortshagen and S. Brovelli, Highly efficient luminescent solar concentrators based on earth-abundant indirect-bandgap silicon quantum dots, *Nat. Photonics*, 2017, **11**, 177–185.

21 S. Sadeghi, H. B. Jalali, R. Melikov, B. G. Kumar, M. M. Aria, C. W. Ow-Yang and S. Nizamoglu, Stokes-shift-engineered indium phosphide quantum dots for efficient luminescent solar concentrators, *ACS Appl. Mater. Interfaces*, 2018, **10**, 12975–12982.

22 G. Liu, R. Mazzaro, Y. Wang, H. Zhao and A. Vomiero, High efficiency sandwich structure luminescent solar concentrators based on colloidal quantum dots, *Nano Energy*, 2019, **60**, 119–126.

23 D. A. Hanifi, N. D. Bronstein, B. A. Koscher, Z. Nett, J. K. Swabeck, K. Takano, A. M. Schwartzberg, L. Maserati, K. Vandewal, Y. van de Burgt, A. Salleo and A. P. Alivisatos, Redefining near-unity luminescence in quantum dots with photothermal threshold quantum yield, *Science*, 2019, **363**, 1199–1202.

24 Y. F. Zhou, D. Benetti, Z. Y. Fan, H. G. Zhao, D. L. Ma, A. O. Govorov, A. Vomiero and F. Rosei, Near infrared, highly efficient luminescent solar concentrators, *Adv. Energy Mater.*, 2016, **6**, 1501913.

25 X. Luo, T. Ding, X. Liu, Y. Liu and K. Wu, Quantum cutting luminescent solar concentrators using ytterbium doped perovskite nanocrystals, *Nano Lett.*, 2019, **19**, 338–341.

26 Y. You, X. Tong, W. Wang, J. Sun, P. Yu, H. Ji, X. Niu and Z. M. Wang, Eco-friendly colloidal quantum dot-based luminescent solar concentrators, *Adv. Sci.*, 2019, **6**, 1801967.

27 L. Dhamo, F. Carulli, P. Nickl, K. D. Wegner, V. D. Hodoroaba, C. Würth, S. Brovelli and U. Resch-Genger, Efficient luminescent solar concentrators based on environmentally friendly Cd-free ternary AIS/ZnS quantum dots, *Adv. Opt. Mater.*, 2021, **9**, 2100587.

28 A. R. M. Velarde, E. R. Bartlett, N. S. Makarov, C. Castañeda, A. Jackson, K. Ramasamy, M. R. Bergren and H. McDaniel, Optimizing the aesthetics of high-performance $CuInS_2$/ZnS quantum dot luminescent solar concentrator windows, *ACS Appl. Energy Mater.*, 2020, **3**, 8159–8163.

29 M. Portnoi, T. J. Macdonald, C. Sol, T. S. Robbins, T. Li, J. Schläfer, S. Guldin, I. P. Parkin and I. Papakonstantinou, All-silicone-based distributed bragg reflectors for efficient flexible luminescent solar concentrators, *Nano Energy*, 2020, **70**, 104507.

30 H. G. Zhao, G. J. Liu, S. J. You, F. V. A. Camargo, M. Zavelani-Rossi, X. H. Wang, C. C. Sun, B. Liu, Y. M. Zhang, G. T. Han,

This journal is © The Royal Society of Chemistry 2023

J. Mater. Chem. A, 2023, **11**, 8950–8960 | **8959**

A. Vomiero and X. Gong, Gram-scale synthesis of carbon quantum dots with a large Stokes shift for the fabrication of eco-friendly and high-efficiency luminescent solar concentrators, *Energy Environ. Sci.*, 2021, **14**, 396–406.

31 J. Wang, J. Wang, Y. Xu, J. Jin, W. Xiao, D. Tan, J. Li, T. Mei, L. Xue and X. Wang, Controlled synthesis of long-wavelength multicolor-emitting carbon dots for highly efficient tandem luminescent solar concentrators, *ACS Appl. Energy Mater.*, 2020, **3**, 12230–12237.

32 Y. Wu, Y. Zhan, W. Xin, W. Cao, J. Li, M. Chen, X. Jiang, J. Wang and Z. Sun, Highly emissive carbon dots/organosilicon composites for efficient and stable luminescent solar concentrators, *ACS Appl. Energy Mater.*, 2022, **5**, 1781–1792.

33 J. C. Chen, H. G. Zhao, Z. L. Li, X. J. Zhao and X. Gong, Highly efficient tandem luminescent solar concentrators based on eco-friendly copper iodide based hybrid nanoparticles and carbon dots, *Energy Environ. Sci.*, 2022, **15**, 799–805.

34 Y. F. Zhou, D. Benetti, X. Tong, L. Jin, Z. M. Wang, D. L. Ma, H. G. Zhao and F. Rosei, Colloidal carbon dots based highly stable luminescent solar concentrators, *Nano Energy*, 2018, **44**, 378–387.

35 H. G. Zhao, Refractive index dependent optical property of carbon dots integrated luminescent solar concentrators, *J. Lumin.*, 2019, **211**, 150–156.

36 G. J. Liu, R. Mazzaro, C. C. Sun, Y. M. Zhang, Y. Q. Wang, H. G. Zhao, G. T. Han and A. Vomiero, Role of refractive index in highly efficient laminated luminescent solar concentrators, *Nano Energy*, 2020, **70**, 104470.

37 M. Wei, F. P. G. de Arguer, G. Walters, Z. Yang, L. N. Quan, Y. Kim, R. Sabatini, R. Quintero-Bermudez, L. Gao, J. Z. Fan, F. Fan, A. Gold-Parker, M. F. Toney and E. H. Sargent, Ultrafast narrowband exciton routing within layered perovskite nanoplatelets enables low-loss luminescent solar concentrators, *Nat. Energy*, 2019, **4**, 197–205.

38 K. B. Cai, H. Y. Huang, M. L. Hsieh, P. W. Chen, S. E. Chiang, S. H. Chang, J. L. Shen, W. R. Liu and C. T. Yuan, Two-dimensional self-assembly of boric acid-functionalized graphene quantum dots: Tunable and superior optical properties for efficient eco-friendly luminescent solar concentrators, *ACS Nano*, 2022, **16**, 3994–4003.

39 Y. T. Lei, Y. F. Li and Z. W. Jin, Photon energy loss and management in perovskite solar cells, *Energy Rev.*, 2022, **1**, 100003.

40 P. Tockhorn, J. Sutter, A. Cruz, P. Wagner, K. Jäger, D. Yoo, F. Lang, M. Grischek, B. Li, J. Z. Li, O. Shargaieva, E. Unger, A. Al-Ashouri, E. Köhnen, M. Stolterfoht, D. Neher, R. Schlatmann, B. Rech, B. Stannowski, S. Albrecht and C. Becker, Nano-optical designs for high-efficiency monolithic perovskite-silicon tandem solar cells, *Nat. Nanotechnol.*, 2022, **17**, 1214–1221.

41 J. Z. Guo, Y. S. Lu, A. Q. Xie, G. Li, Z. B. Liang, C. F. Wang, X. N. Yang and S. Chen, Yellow-emissive carbon dots with high solid-state photoluminescence, *Adv. Funct. Mater.*, 2022, **32**, 2110393.

42 S. Y. Song, L. Z. Sui, K. K. Liu, Q. Cao, W. B. Zhao, Y. C. Liang, C. F. Lv, J. H. Zang, Y. Shang, Q. Lou, X. G. Yang, L. Dong, K. J. Yuan and C. X. Shan, Self-exothermic reaction driven large-scale synthesis of phosphorescent carbon nanodots, *Nano Res.*, 2021, **14**, 2231–2240.

43 Q. Zhang, R. Wang, B. Feng, X. Zhong and K. K. Ostrikov, Photoluminescence mechanism of carbon dots: Triggering high-color-purity red fluorescence emission through edge amino protonation, *Nat. Commun.*, 2021, **12**, 6856.

44 L. ZdraZil, S. Kalytchuk, K. Hola, M. Petr, O. Zmeskal, S. Kment, A. L. Rogach and R. Zboril, A carbon dot-based tandem luminescent solar concentrator, *Nanoscale*, 2020, **12**, 6664–6672.

45 V. I. Klimov, T. A. Baker, J. Lim, K. A. Velizhanin and H. McDaniel, Quality factor of luminescent solar concentrators and practical concentration limits attainable with semiconductor quantum dots, *ACS Photonics*, 2016, **3**, 1138–1148.

46 W. Ma, W. Li, R. Liu, M. Cao, X. Zhao and X. Gong, Carbon dots and AIE molecules for highly efficient tandem luminescent solar concentrators, *Chem. Commun.*, 2019, **55**, 7486–7489.

47 Z. Wang, X. Zhao, Z. Guo, P. Miao and X. Gong, Carbon dots based nanocomposite thin film for highly efficient luminescent solar concentrators, *Org. Electron.*, 2018, **62**, 284–289.

48 M. J. Talite, H. Y. Huang, Y. H. Wu, P. G. Sena, K. B. Cai, T. N. Lin, J. L. Shen, W. C. Chou and C. T. Yuan, Greener luminescent solar concentrators with high loading contents based on in situ cross-linked carbon nanodots for enhancing solar energy harvesting and resisting concentration induced quenching, *ACS Appl. Mater. Interfaces*, 2018, **10**, 34184–34192.

49 H. Zhao, G. Liu and G. Han, High-performance laminated luminescent solar concentrators based on colloidal carbon quantum dots, *Nanoscale Adv.*, 2019, **1**, 4888–4894.

50 H. Hernandez-Noyola, D. H. Potterveld, R. J. Holt and S. B. Darling, Optimizing luminescent solar concentrator design, *Energy Environ. Sci.*, 2012, **5**, 5798–5802.

51 F. Mateen, M. Ali, S. Y. Lee, S. H. Jeong, M. J. Ko and S. K. Hong, Tandem structured luminescent solar concentrator based on inorganic carbon quantum dots and organic dyes, *Sol. Energy*, 2019, **190**, 488–494.

52 F. Mateen, M. Ali, H. Oh and S. K. Hong, Nitrogen-doped carbon quantum dot based luminescent solar concentrator coupled with polymer dispersed liquid crystal device for smart management of solar spectrum, *Sol. Energy*, 2019, **178**, 48–55.

8960 | *J. Mater. Chem. A*, 2023, **11**, 8950–8960

This journal is © The Royal Society of Chemistry 2023